Supplementary Information for

Probing Longitudinal Carrier Transport in Perovskite Films via Modified Transient Reflection Spectroscopy

Shengli Zhao,[a, b] Jing Leng,[b] Shiping Wang,[b, c] Xianchang Yan,[b] Zixi Yin,[b] Yanfeng Yin,[b] Jun Zhang,[a, d*] Shengye Jin[b*]*

[a] State Key Laboratory of Heavy Oil Processing, College of Chemical Engineering, China University of Petroleum (East China), Qingdao 266580, China.

[b] State Key Laboratory of Molecular Reaction Dynamics, Dalian Institute of Chemical Physics, Chinese Academy of Sciences, Dalian 116023, China.

[c] Department of Chemistry, School of Science, Tianjin University, Tianjin 300354, China.

[d] College of Materials Science and Engineering, China University of Petroleum (East China), Qingdao 266580, China.

Preparation of MAPbI$_3$ perovskite thin films.

The perovskite thin films were prepared from modified nonstoichiometric precursor. For large-grain films, methylammonium iodide (MAI), lead iodide (PbI$_2$), and methylammonium chloride (MACl) (MAI: PbI$_2$: MACl =1:1:0.2) were dissolved in N-Methyl-2-pyrrolidone (NMP) and gamma- Butyrolactone (GBL) (NMP: GBL=7: 3, volume ratio) to form 55 wt% and 60 wt% precursor solutions, respectively. In order to prepare MAPbI$_3$ films with different thicknesses, 55 wt% MAPbI$_3$ precursor solutions was span at 4000 rpm, 3000 rpm, 2000 rpm for 25 s, and 60 wt% MAPbI$_3$ precursor solutions was span at 3000 rpm, 2000 rpm for 25 s respectively. After spin-coating, these films were promptly transferred into abundant diethyl ether (DEE) solution for 90 s to finish the crystallization process and further annealed at 150 ℃ for 15 min with a Petri dish covered. The thickness of spun films were 550, 753, 1100, 1200 and 1540 nm, respectively. For small-grain films, 60 wt% precursor (MAI: PbI$_2$=1: 1) and precursor (MAI: PbI$_2$: MACl =1:1:0.1) solutions were used. All films

were obtained by spin-coating their precursor solutions on FTO glasses followed by the same ether bathing and thermal annealing in air.

Transient absorption (TA) measurement.

The femtosecond TA spectrometer is based on a Yb:KGW laser system (1030 nm, 100 kHz; Light Conversion Ltd.), nonlinear frequency mixing techniques and the Femto-TA100 spectrometer (Time-Tech Spectra LLC). Briefly, the fundamental output at 1030 nm was split in two parts. One part was introduced to a noncollinear optical parametric amplifier to generate a certain wavelength for pump beam. The other was focused onto a YAG crystal to generate continuum white light (550–950 nm) as probe beam. The probe beam was focused with a parabolic reflector onto the sample and the transmitted probe beam was then collimated and focused into a fiber-coupled spectrometer with CMOS sensors. The intensity of the pump pulse used in the experiment was controlled by a variable neutral-density filter wheel. The delay between the pump and probe pulses was controlled by a motorized delay stage. The pump pulses were chopped by a synchronized chopper at 5 KHz and the absorbance change was calculated with two adjacent probe pulses (pump-blocked and pump-unblocked).

Normal and back-excitation transient reflection (TR) measurement.

The TR measurements were performed by using the same pump–probe transient spectrometer with a modified optical path, where the detection signal is the reflected probe beam. Briefly, the fundamental output from a Yb:KGW laser (1030 nm, 100 kHz; Light Conversion Ltd.) was split in two parts. One part was introduced to a noncollinear optical parametric amplifier to generate a certain wavelength for pump beam. The other was focused onto a YAG crystal to generate continuum white light (550–950 nm) as probe beam. The probe beam was focused with a parabolic reflector onto the sample and the reflected probe beam was then collimated and focused into a fiber-coupled spectrometer. The incident angle for the pump beam is around 0° and that for the probe beam is around 45°. For normal TR measurement, the pump and

probe beams impinge on the same side of the sample and were spatially overlapped on the sample surface. For back-excitation TR measurement, the pump and probe beams respectively impinge on both side of the sample. All experiments were performed at room temperature.

(a) film 1   **(b) film 2**   **(c) film 3**

(d) film 4   **(e) film 5**
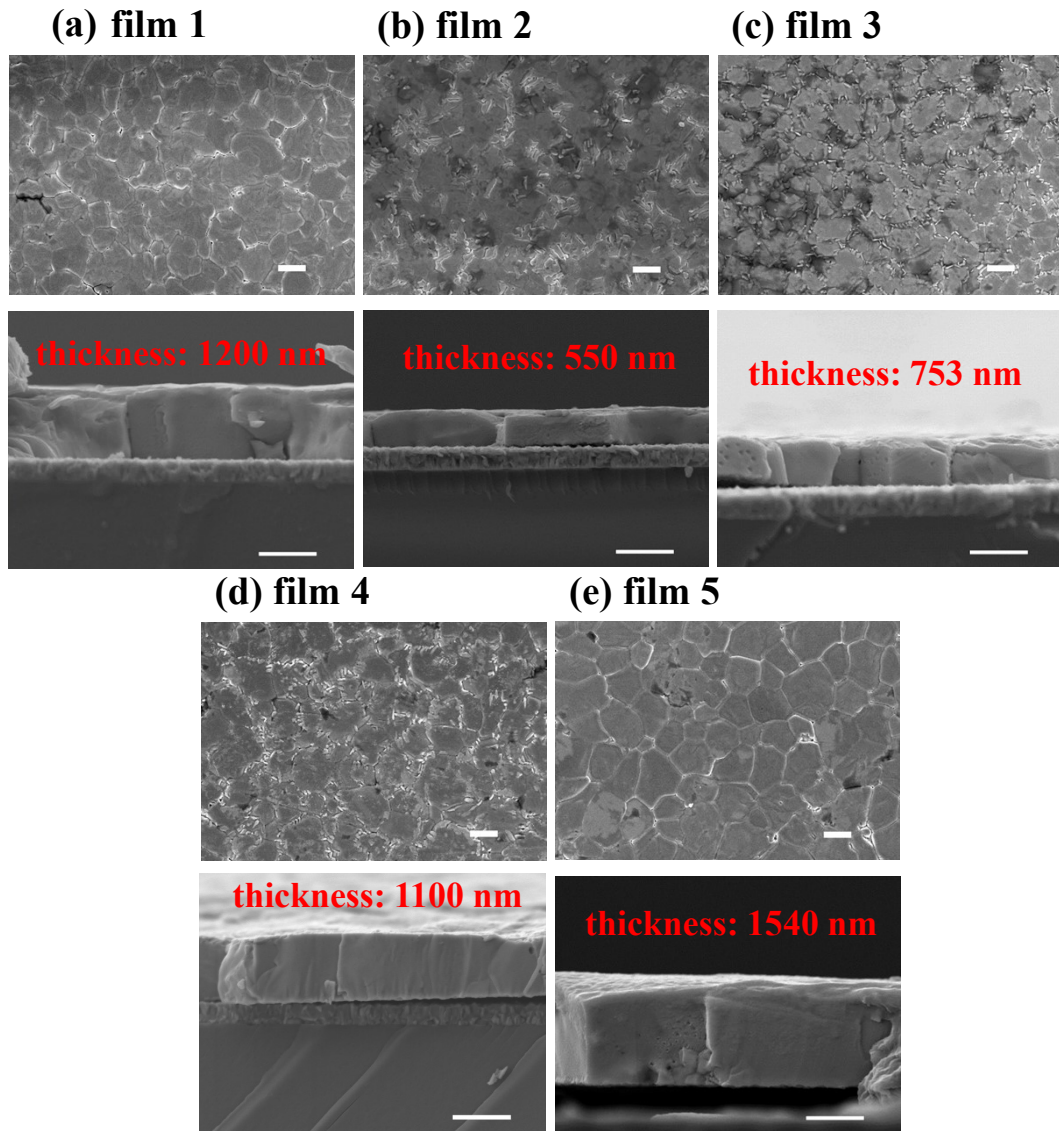
Fig. S1 Top-view (upper panels) and cross-sectional (lower panels) SEM images of five large-grain MAPbI$_3$ films with different thicknesses of (a) 1200 nm, (b) 550 nm, (c) 753nm, (d) 1100 nm and (e) 1540 nm. Scale bar: 2 μm for top-view images, 1 μm for cross-sectional images.

(a) film 6

(b) film 7

(c) film 8

(d) film 9
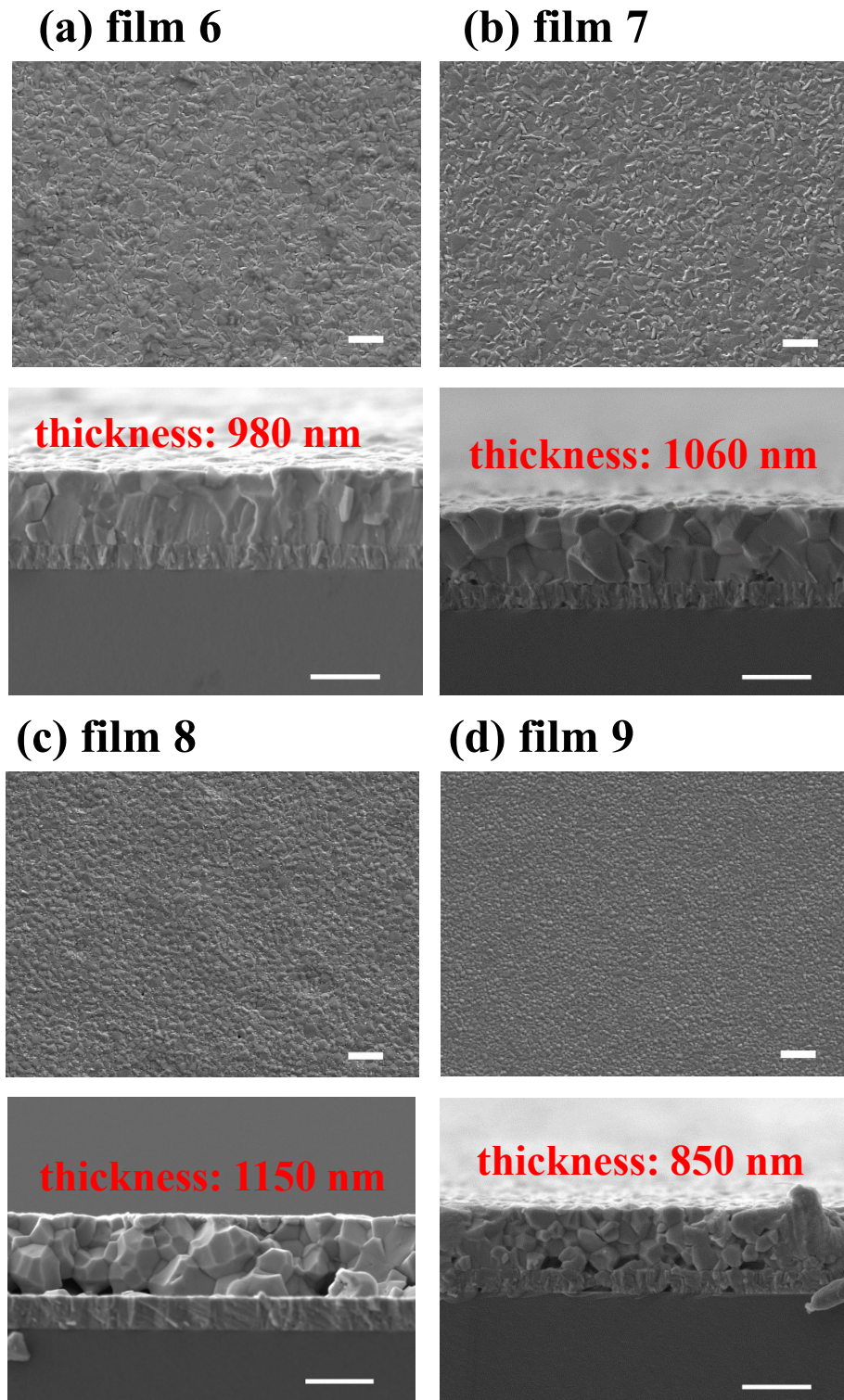
Fig. S2 Top-view (upper panels) and cross-sectional (lower panels) SEM images of four small-grain MAPbI$_3$ films with different thicknesses of (a) 980 nm, (b) 1060 nm, (c) 1150nm, (d) 850 nm. Scale bar: 2 µm for top-view images, 1 µm for cross-sectional images.
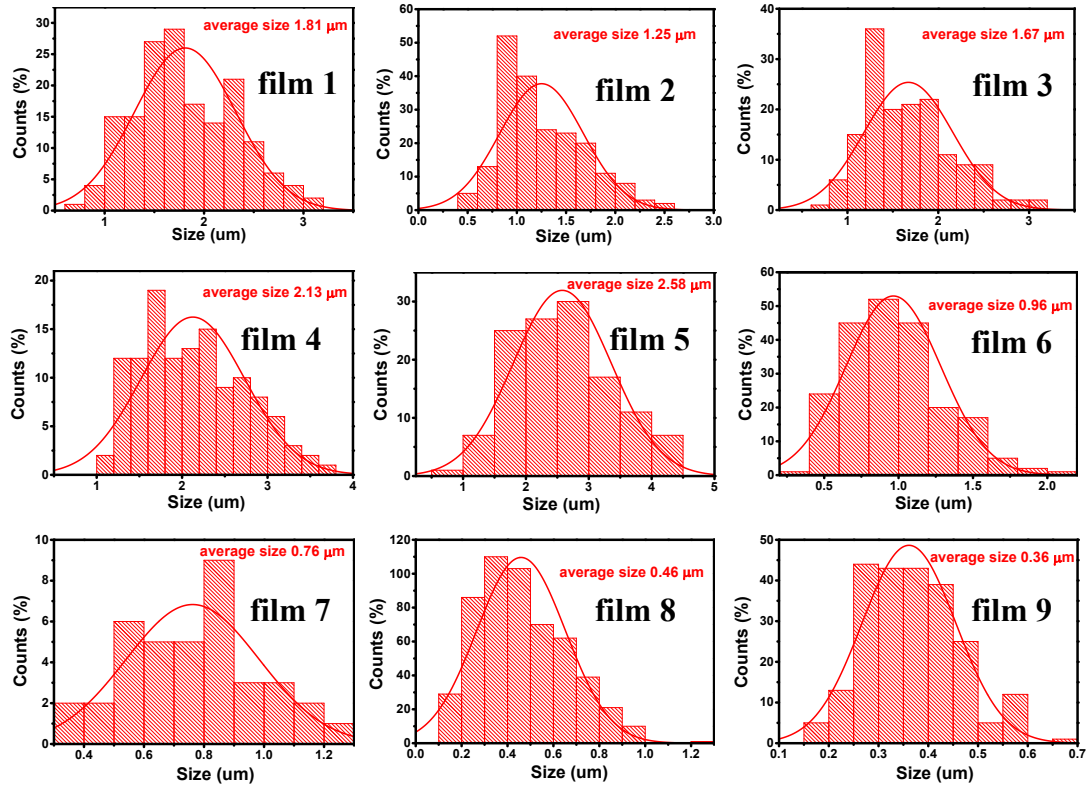
Fig. S3 Lateral grain size statistical distribution of all as-prepared MAPbI$_3$ films determined from their top-view SEM images as shown in Fig. S1 and S2.
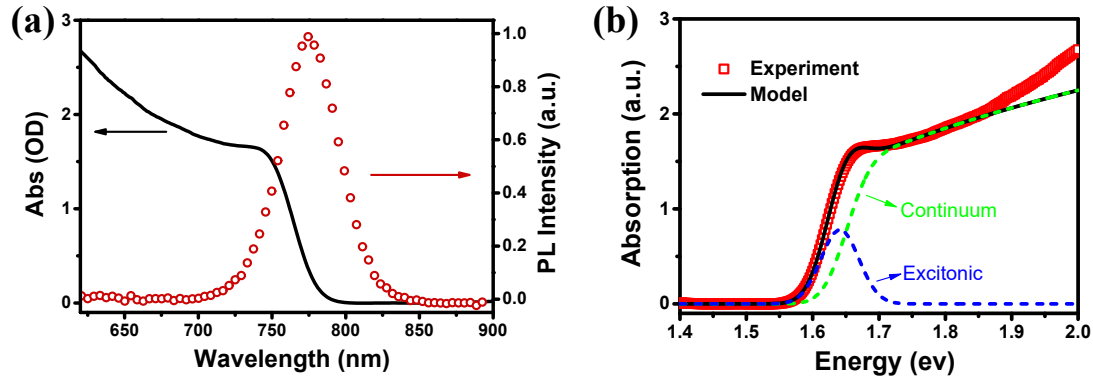
Fig. S4 (a) The UV−Vis absorption and PL spectra of a typical MAPbI$_3$ film (film 1) as shown in Fig. S1a. (b) The measured linear absorption spectra (red squares) of the film and its corresponding simulations (black line) based on Elliott's model. The blue and green dashed lines represent the excitonic and continuum contributions to the total absorption. For photon energies greater than ~1.8 eV, the absorption no longer follows Elliott's model since the contribution from higher energy bands is ignored.
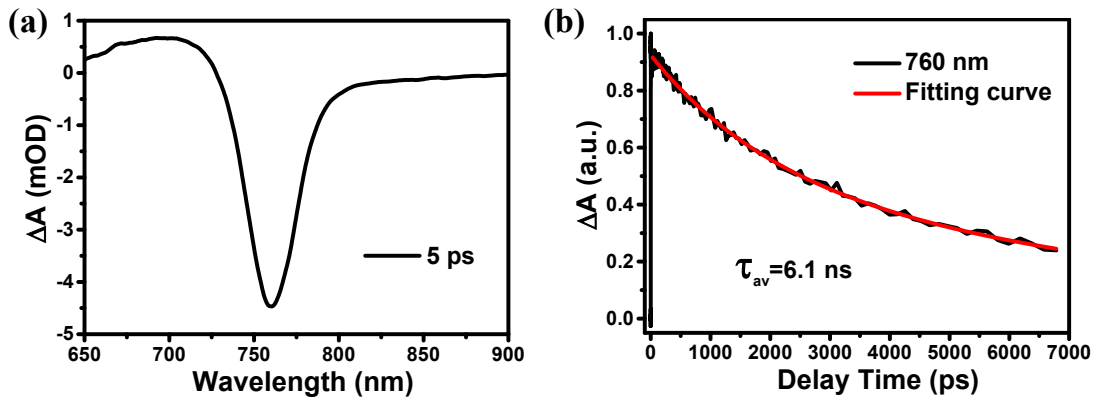
Fig. S5 (a) TA spectra measured in MAPbI$_3$ film at a delay time of 5 ps. (b) TA kinetics probed at 760 nm in the MAPbI$_3$ film. The red line is a bi-exponential fit of TA kinetics, yielding the average bulk carrier lifetime of $\tau = 6.1$ ns.
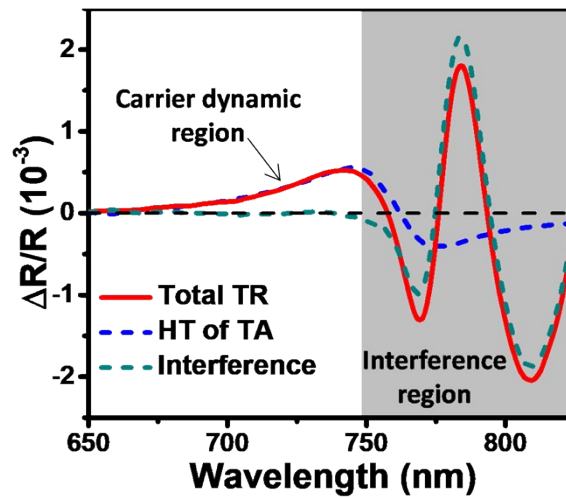

Fig. S6 The TR spectra recorded at 2100 ps delay under back-excitation at 635 nm in the same perovskite film (film 1) as used in Fig. 2. The Hilbert transform of TA spectrum (blue trace) and the interference signal (green trace) deconvolved from total TR spectrum are also shown. The spectral features in the grey shaded region result from the interference of the reflected probe beam from both the front and back surface of thin film.
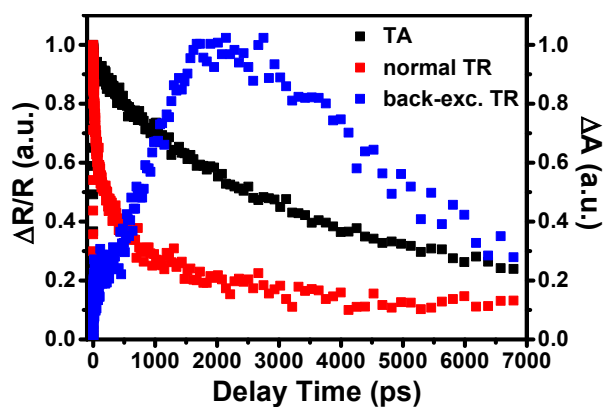
Fig. S7 The comparison of the normalized TR kinetics probed at 720 nm in typical perovskite film (film 1) as shown in Fig. S1a under normal- (red trace) and back-excitation (blue trace) TR modes respectively, as well as its TA kinetics (black trace) probed at 760 nm of the perovskite film.
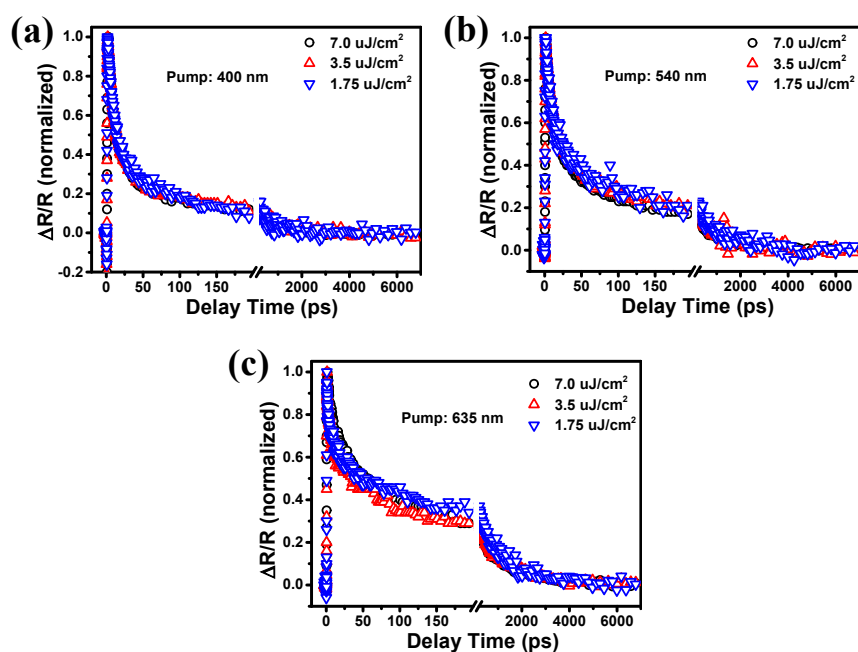
Fig. S8 The normal TR kinetics probed at 720 nm in typical perovskite film (film 1) as shown in Fig. S1a with different excitation fluence under indicated pump wavelength at (a) 400nm, (b) 540nm, (c) 635nm, respectively. These data indicate that the higher-order recombination can be avoided and thus these TR kinetics are independent of the excitation intensities when the excitation fluence $< 7 \mu J/cm^2$.
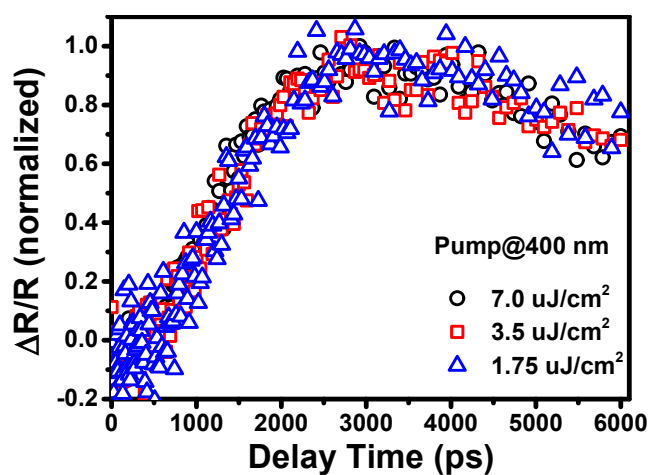
Fig. S9 The back-exc. TR kinetics probed at 720 nm in perovskite film with 1200-nm thickness under 400 nm excitation with different fluences. These data indicate that the TR kinetics is independent of the excitation intensities when the excitation fluence < 7 μJ/cm^2 and thus the effect of high-order recombination in this case is negligible.
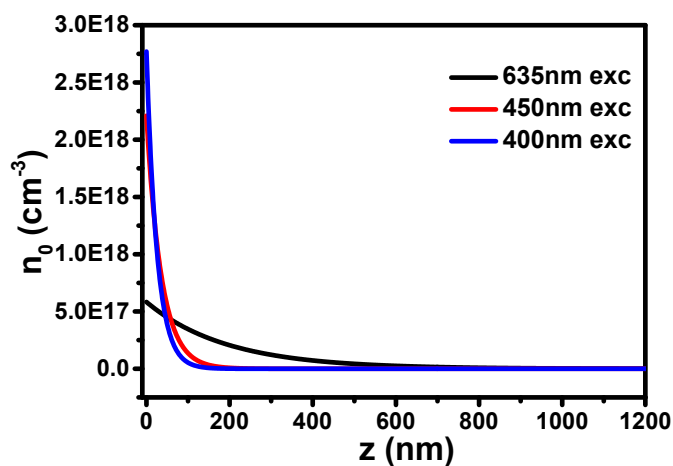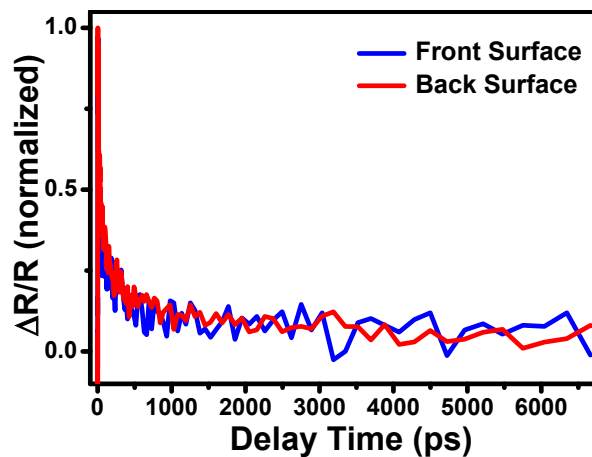

**Fig. S10** The simulated initial carrier distributions along the film thickness direction at different excitation wavelengths.
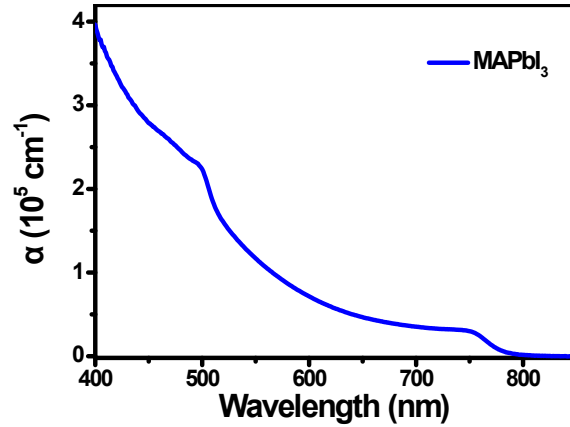
Fig. S11   The measured absorption coefficient of MAPbI$_3$ perovskite film as a function of wavelength.

Fig. S12   Normal TR kinetics of the typical perovskite film as shown in Fig. S1a. The kinetics are extracted from the normal TR spectra collected from the front surface (blue trace) and the back surface (red trace). The back surface is the interface between the perovskite film and FTO glass. The consistency of the two kinetic traces suggests that the surface recombination velocity (S) for the front and back surfaces are similar.
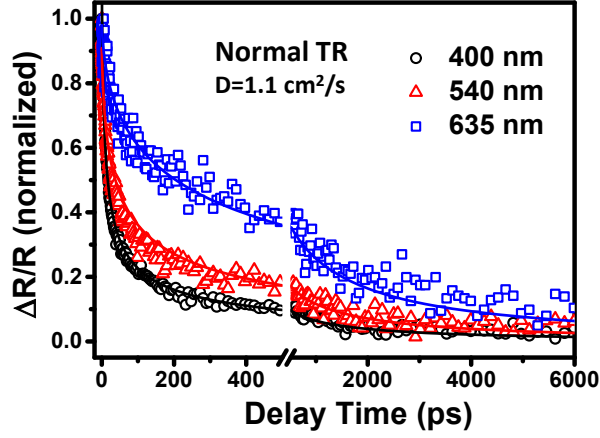
Fig. S13 The normal TR kinetics probed at 720 nm in the same film with larger grains as in Fig. 3a (film 1) under excitation at indicated wavelengths. The solid lines are their global fits according to the diffusion model discussed in the main text.
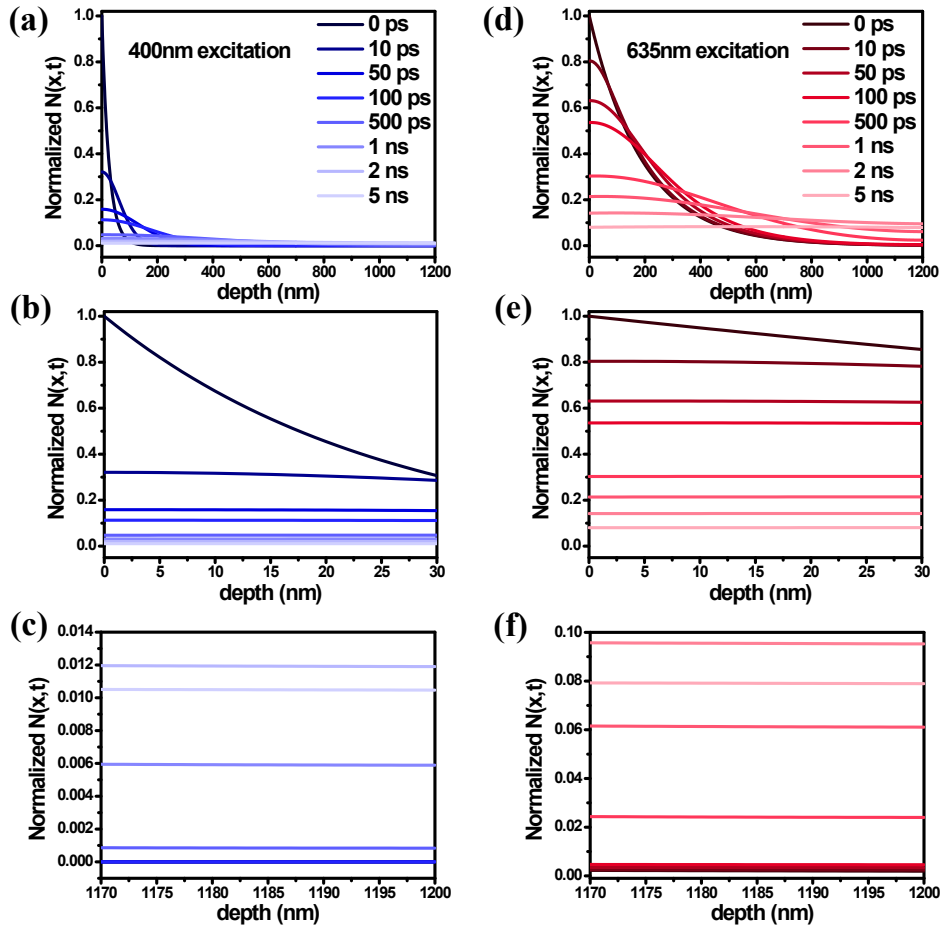

Fig. S14 Simulated longitudinal carrier distribution at indicated delay times in 1200-nm-thickness perovskite film with D=1.5 cm²s⁻¹, S=2000 cm/s and $k_1=10^8$ s⁻¹. The excitation wavelengths are indicated in the figures. The top row (a, d) shows the

carrier distribution in the whole film. The middle row (b, e) shows the carrier distribution in the effective detection depth (~30 nm) of the front surface. The bottom row (c, f) shows the carrier distribution in the effective detection depth of the back surface. It is evident that the carrier density at the front surface exhibits an uneven distribution during initial delays after excitation, while that at the back surface always shows a uniform distribution during any delays.
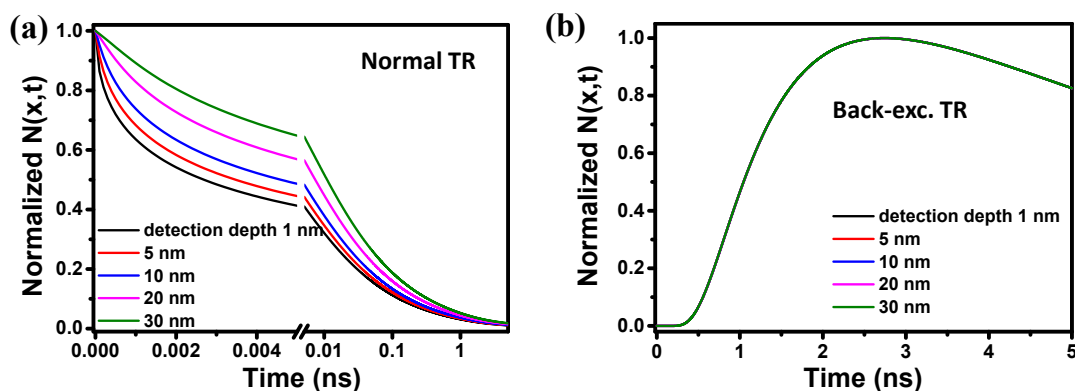

Fig. S15 The simulated TR kinetics in 1200-nm-thickness perovskite film (with $D=1.5$ cm^{2}s^{-1}, $S=2000$ cm/s and $k_1=10^8$ s^{-1}) under 400 nm excitation by using different detection depth in (a) normal- and (b) back-excitation TR mode, respectively. The remarkable difference of simulated TR kinetics among different detection depths in normal TR mode suggests that the detection depth necessarily influences their fitting results, while the consistency of TR kinetics among different detection depths in back-excitation TR mode suggests that the detection depth should not affect their fitting results.
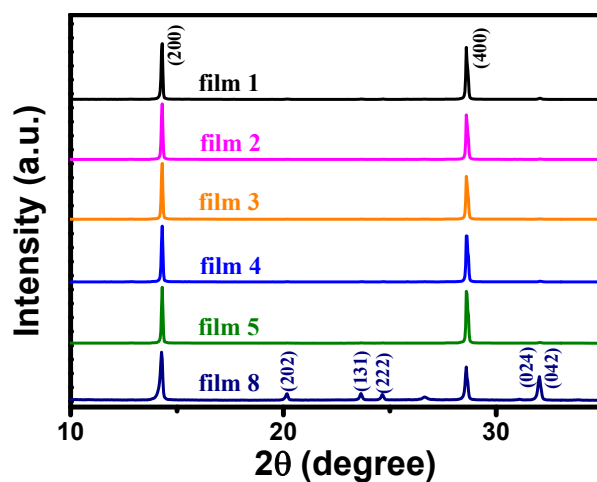
Fig. S16 XRD patterns of five large-grain MAPbI$_3$ thin films (film 1-5) and a small-grain film (film 8), as shown in Fig. S1 and S2c. For large-grain films, their XRD patterns only exhibit two very strong diffraction peaks, suggesting that each grain within the film is highly oriented and high crystallinity. It is quite different from small-grain film where other diffraction peaks from different crystallographic planes also appear because the small grains prefer random orientation.
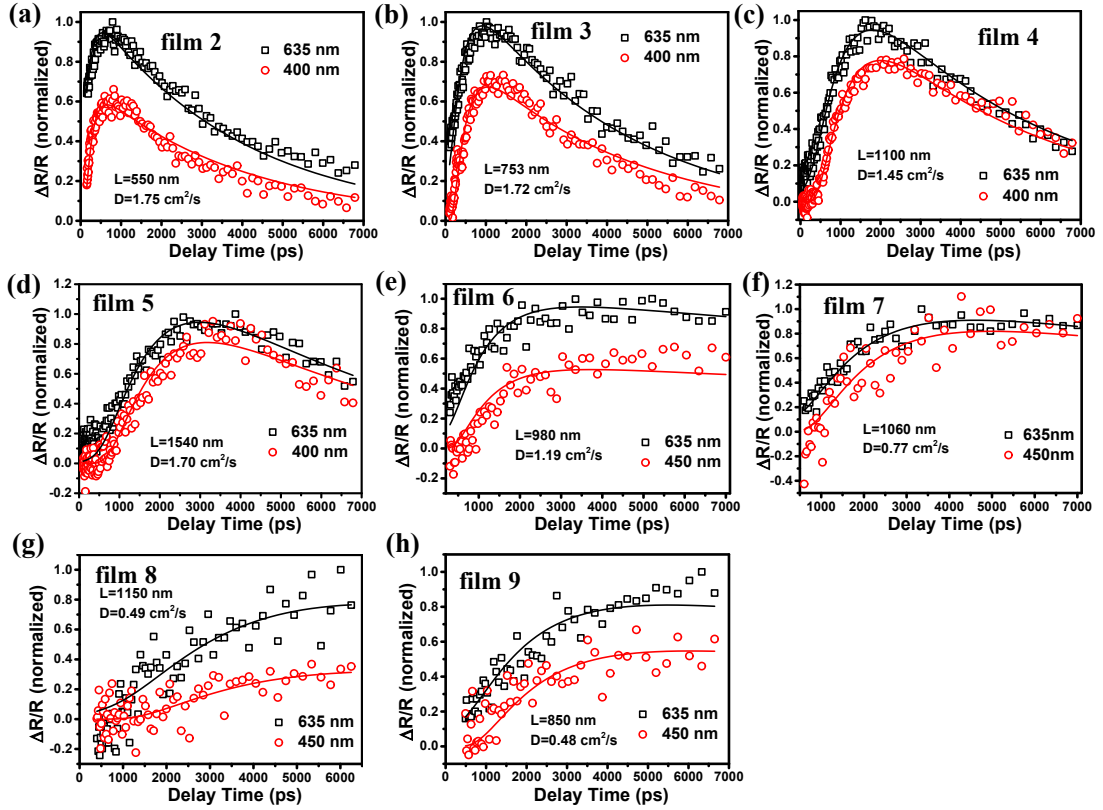
Fig. S17 The back-excitation TR kinetics probed at 720 nm in various MAPbI$_3$ perovskite films (film 2-9) with different thicknesses and grains under excitation at the indicated pump wavelength. The solid lines are their global fits according to the diffusion model discussed in the main text and the detailed fitting results are summarized in Table S1. Note that the bulk carrier lifetimes used during the fitting for the films with large grains (i.e., film 1-5) are extracted from their TA kinetics due to their very short lifetimes, while those for the films with small grains (i.e., film 6-9) are extracted from their measured PL kinetics (see Fig. S18b) due to their relatively long lifetimes.
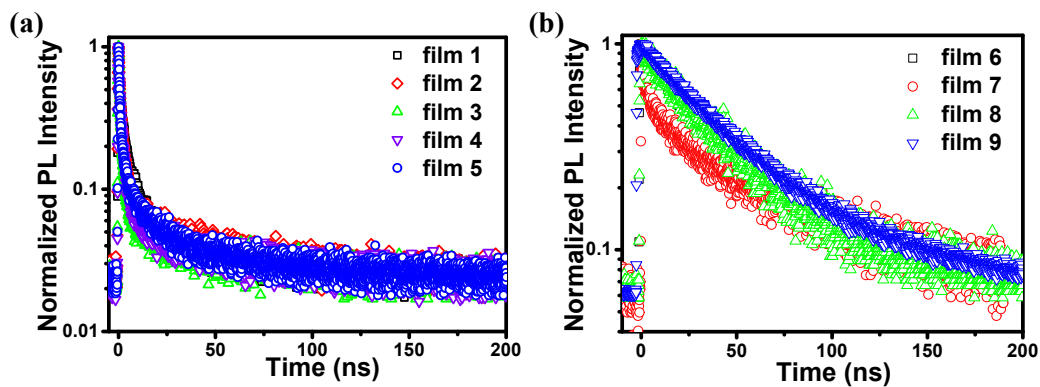
Fig. S18 Comparison of PL kinetics collected at 770 nm in various perovskite films with (a) large grains (film 1−5) and (b) small grains (film 6-9).

Table S1. Fitting parameters for back-excitation TR kinetics of different perovskite films shown in Fig. 3a and S17. (D and S are set as free fitting parameters.)

film No.	Thickness (nm)	Grain size (um)	R	D (cm²s⁻¹)	S (cm s⁻¹)
film 1	1200	1.81	0.66	1.52	5807.5
film 2	550	1.25	0.44	1.75	3035.5
film 3	753	1.67	0.45	1.72	3669.0
film 4	1100	2.13	0.51	1.45	4913.0
film 5	1540	2.58	0.59	1.70	1611.2
film 6	980	0.96	1.02	1.19	0*
film 7	1060	0.76	1.39	0.77	1213*
film 8	1150	0.46	2.5	0.49	0*
film 9	850	0.36	2.36	0.48	0*

* Note: The S values obtained for four films (film 6-9) with small grains are of insignificance due to the absence of the evident decay process in their TR kinetics (see Fig. S17).